On the Vortex Flow Phenomena of a Triple-Delta-Wing Aircraft Configuration in Transonic Flows

Thomas G. Schmidt*, Patrick Hartl†, Reinhard Geisler‡, Robert Konrath§, Marc Braune¶
German Aerospace Center (DLR), 37073 Göttingen, Germany

The present work focuses on the experimental investigation and characterization of vortex-flow phenomena of a generic triple-delta-wing configuration, like the DLR-F23 aircraft, under various transonic speeds and angles of attack. This experimental study is conducted at the Transonic Wind Tunnel in Göttingen, which allows for the exploration of multiple transonic flow regimes and several angles of attack using two advanced flow visualization techniques, namely stereoscopic particle-image velocimetry and fast-response, unsteady pressure-sensitive paint. From these flow visualizations, it is found that three distinct vortex systems develop over the surface of the DLR-F23 wing, namely an inboard, midboard, and outboard vortex, which respectively develop from the model's forebody, strake, and main wing. These vortical structures are strongly dependent on the flow conditions, whether this concerns low-to-high transonic conditions and/or the wing's angle of attack. In particular at higher transonic flows, significant compressible effects, such as shock fronts, develop that noticeably affect the vortices' characteristics and behavior, including - but not limited to - vortex-vortex and vortex-shock interactions, their breakdown and/or merging. Upon these observations, future work may be directed towards further exploring these complex vortex-dominated flows under trans- and even supersonic flow conditions, whether this being done through dedicated experimental efforts and/or by employing advances numerical means. All this would allow developing more efficient and high performant triple-delta-wing aircraft configurations that could operate robustly across a wide range of flight conditions (i.e., Mach numbers, pitch angles).

I. Nomenclature

A_{ref}	=	reference surface area (m^2)
l_μ	=	reference length (m)
Ma	=	Mach number (-)
Re	=	Reynolds number (-)
s	=	wing halfspan (m)
T	=	total temperature (K)
u_∞	=	free-stream velocity (m/s)
u, v, w	=	Velocity components in x, y, and z direction (m)
x, y, z	=	Cartesian coordinates (m)
α	=	pitch angle (or angle of attack) ($^\circ$)
ω_x	=	streamwise vorticity in x-direction (1/s)
φ	=	sweep angle ($^\circ$)
ρ	=	air density (kg/m^3)
CFD	=	computational fluid dynamics
DLR	=	German Aerospace Center
DNW	=	German-Dutch Wind Tunnels
IBV	=	inboard vortex
MBV	=	midboard vortex

*Research Associate, Institute of Aeroelasticity, tg.schmidt@dlr.de
†Research Associate, Institute of Aeroelasticity, patrick.hartl@dlr.de
‡Research Associate, Institute of Aerodynamics and Flow Technology, reinhard.geisler@dlr.de
§Senior Scientist, Institute of Aerodynamics and Flow Technology, robert.konrath@dlr.de, AIAA Senior Member
¶Lead Scientist, Institute of Aeroelasticity, marc.braune@dlr.de

OBV = outboard vortex
PIV = particle-image velocimetry
TWG = Transonic Wind Tunnel Göttingen
uPSP = unsteady pressure-sensitive paint

II. Introduction

High agility and flight speed are pivotal characteristics that are sought after in modern multi-delta-wing aircraft configurations. While traditional delta wing planforms were specifically focused on in the past [1–7], multi-delta wing configurations emerged as a promising design variation to optimize aerodynamic performance characteristics. In particular, special attention is now paid to novel triple-delta-wing designs, which consist of multiple highly-swept leading edges. These induce complex vortex-flow systems, which travel downstream along the wing surface and possibly interact with one another. While the benefit of these vortices lies in their ability to retain high lift and aerodynamic stability, they are highly susceptible to the flow conditions (i.e., Mach number, Ma, and pitch angle, α), especially what concerns the transonic regime where compressibility effects would occur.

Past research on triple-delta-wing aircrafts has provided a good understanding of their aerodynamics, particularly concerning the vortex dynamics and lift enhancement at subsonic speeds [8–15]. Under such subsonic conditions, the flow field is primarily characterized by two vortex systems, namely one developing at the most inboard wing section (hence, inboard vortex, or IBV) and another forming further downstream at the midboard kink between highly and moderately swept leading edges (hence, midboard vortex, or MBV) [10, 11]. These vortical structures are strongly driven by the leading-edge geometry, particularly its sweep angles, which would not only influence the vortices' strength, but also their behavior (e.g., trajectory) further downstream. More specifically, they are shown to interact with one another as they travel downstream over the wing surface, possibly merging and/or breaking down. Similar observations were made in another work on the matter [13], whose combined experimental and numerical investigations emphasized the sensitivity of the vortex systems' behavior on the geometric parameters, including - but not limited to - the wing planform, chord ratios, and leading-edge sweep angles. Specifically the sweep angle of the leading edges, being either relatively vaguely considered non-slender ($\varphi < 65°$) or slender ($\varphi > 65°$), are known to drive the vortex-breakdown type [4, 8, 16–18]. For instance, non-slender leading-edge wings are typically characterized by a gradual transition from a jet-type (i.e., vortex-core velocity $u_{\text{core}}/U_\infty > 1$) to a wake-type ($u_{\text{core}}/U_\infty < 1$) vortex structure. On the other hand, slender leading-edge wings are characterized by a rather suddden breaking down of the vortex systems, featuring abrupt deceleration of the axial flow velocity in the vortex core (up to flow reversal, i.e., $u_{\text{core}}/U_\infty < 0$). Notably, the vortex breakdown can be further characterized by different behaviors, such as being of spiral- or bubble-type [18–20].

Beyond the subsonic flight regime, modern triple-delta-wing aircrafts frequently operate in transonic flow conditions, thus being affected by unsteady compressibility effects, such as shock interactions. As a result, research efforts have been devoted to expand the understanding of vortex flow phenomena pertaining to such triple-delta-wing configurations in transonic flows, among which recent computational fluid dynamics (CFD) simulations based on Unsteady Reynolds-Averaged Navier Stokes (URANS) [8, 9, 21–23] and/or Delayed Detached Eddy Simulations (DDES) [21, 23, 24]. Their results revealed that a triple-delta-wing aircraft exposed to transonic flow conditions exhibits even more complex flow physics due to the interplay between the sensitive vortex systems (and their inherent instabilities) and compressible effects (i.e., shocks) [21, 25]. In other words, shock waves affect - and possibly trigger - the instabilities of these vortices, leading to their breakdown or merging, which may ultimately be referred to as vortex-shock, or even vortex-vortex, interactions.

While the above literature provides valuable insights towards the understanding of vortex flow phenomena for transonic conditions, there still remains a lack of experimental investigations on the subject, primarily due to the complexity and limited accessibility of transonic wind tunnel facilities. To the authors' best knowledge, only one recent experimental work exists that explored a similar aircraft configuration in transonic flows [23]. This study focused on investigating both experimentally and numerically a multi-swept delta wing configuration, namely the DLR-F22 model, in the transonic regime, respectively using particle-image velocimetry (PIV) as well as URANS and Improved Delayed Detached Eddy Simulations (IDDES) computations. While an overall acceptable agreement between the numerical results and the experimental data (for selected cases) is observed, only the computationally more expensive IDDES simulations could sufficiently resolve the complex flow phenomena for the transonic conditions (e.g., Ma = 0.85). The complexity of resolving the interplay between the non-trivial vortex structures and the unsteady, compressible effects induced by the transonic flow is also seen in other numerical computations, which revealed how the vortex-shock interaction is strongly dependent on the turbulence model accurately capturing the vortices' breakdown onset [26, 27].

Upon the above insights, there exists a need for experimental data of a generic triple-delta-wing configurations tested in transonic flow conditions. While extensive experimental works have focused on subsonic flows, dedicated investigations in the transonic regime, especially those utilizing advanced flow visualization techniques, such as stereoscopic particle-image velocimetry (stereo-PIV) or unsteady pressure-sensitive paint (uPSP), remain scarce. Aside from that, most of the existing transonic studies to date relied heavily on CFD computations without sufficient experimental validation to compare with. The absence of detailed experimental results from wind tunnel campaigns further limits the ability to refine or validate existing numerical models, leaving potentially critical aspects of transonic vortex dynamics underexplored.

The present work aims to address this gap by experimentally investigating the (unsteady) vortex flow phenomena of a triple-delta-wing configuration, namely the DLR-F23 model, over a wide range of flow conditions, including sub- and transonic flow regimes as well as various aircraft pitch angles. This is achieved via state-of-the-art flow visualization techniques, like stereo-PIV and uPSP. The novel contribution of this work lies in leveraging both these experimental techniques to characterize and analyze a triple-delta wing's vortex flow phenomena in the transonic regime, which may also serve as validation data for further numerical explorations.

The paper is structured as follows: Section III describes the experimental means and setup, which are employed throughout this test campaign, while the corresponding results are discussed in Section IV. Finally, some conclusions and perspectives are outlined in Section V.

III. Experimental Means and Setup

A. Experimental facility

The experimental campaign is conducted in the so-called Transonic Wind Tunnel Göttingen (DNW-TWG), see Fig. 1, administrated by the German-Dutch Wind Tunnels (DNW). The DNW-TWG is a closed-vein, hard-walled wind tunnel of Göttinger type whose test section extends over 1.0 m (W) × 1.0 m (H) × 4.5 m (L). Notably, this tunnel can be equipped with three different test sections, among which one employing perforated walls that are specifically designed reach high transonic flow regimes. This particular test section can achieve Mach numbers of Ma = 0.30 to 1.20, the higher end of which can only be reached due to the additional suction provided by the perforation in the walls. Besides, this section is enclosed in a pressurized chamber, whose pressure and Reynolds number can be adjusted independently of the Mach number, enabling a total pressure range of p_{tot} = 30 kPa to 150 kPa. The turbulence level inside the test section is seen to vary between 0.10 % and 0.25 %, depending on the flow conditions.

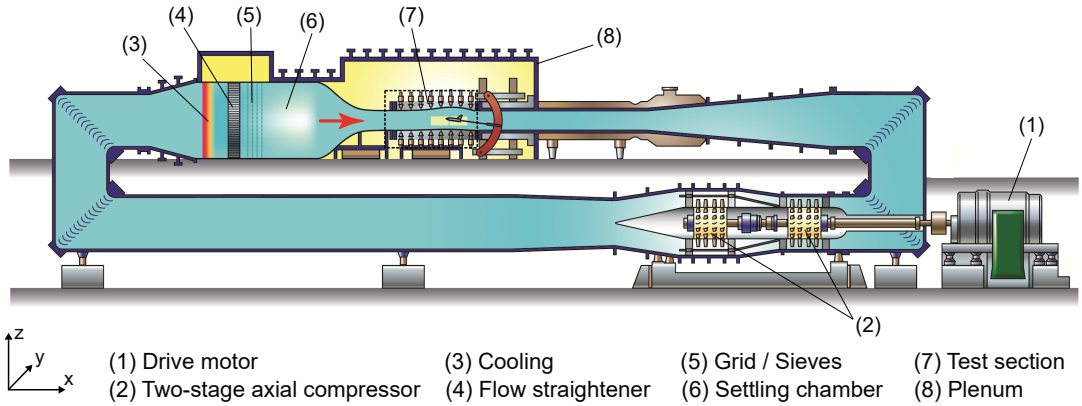

Fig. 1 Schematic of the transonic wind tunnel (DNW-TWG) used throughout this experimental campaign.

B. Triple-delta-wing configuration - the DLR-F23

The aircraft model relies on a novel triple-delta-wing configuration developed in the project *Diabolo* at the German Aerospace Center (DLR), namely the DLR-F23 configuration - cf. Fig. 2. This DLR-F23 aircraft comes as a generic wing-fuselage half-span wind tunnel model with an ogival consine-chined forebody that is mounted to the tunnel's

wall via a peniche (see Fig. 3), to minimize any bias coming from the boundary layer. In particular, the DLR-F23 model is composed of three main sections, corresponding to the front leading-edge vortex controller (LEVCON), the middle strake, and the rear main wing, their leading edge being respectively swept by $\varphi_1 = 45°$, $\varphi_2 = 75°$, and $\varphi_3 = 45°$. Notably, three characteristics lengths describe the DLR-F23 configuration, namely its wing root chord ($c_{\mathrm{r,w}} = 0.575\,\mathrm{m}$), its total length ($l_{\mathrm{m}} = 0.862\,\mathrm{m}$), and its half span ($s_{\mathrm{m}} = 0.420\,\mathrm{m}$) - cf. Fig. 2. In addition, the model has a mean aerodynamic chord of $l_\mu = 0.382\,\mathrm{m}$ and reference surface area of $A_{\mathrm{ref}} = 0.133\,\mathrm{m}^2$. For further details regarding the DLR-F23 model geometry, the reader is referred to past works on the matter [28, 29].

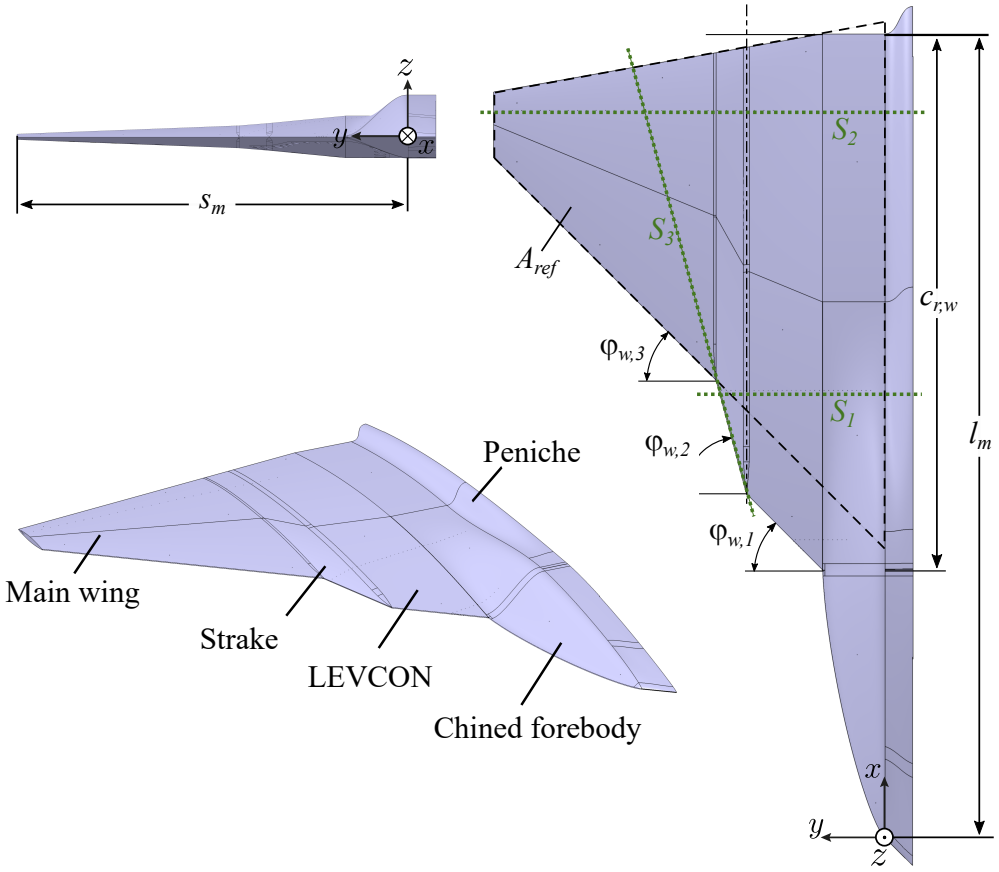

Fig. 2 Schematics of the DLR-F23 configuration, shown from front (top-left), top (right), and isometric views (bottom-left).

C. Measurement techniques

The flow field around and over the wing's surfaces are visualized using steady stereoscopic particle-image velocimetry (stereo PIV) and fast-response, unsteady pressure-sensitive paint (uPSP), which have been performed one after another in separate experimental tests.

To characterize the three-dimensional flow field around the DLR-F23 model, stereo PIV is employed. This experimental technique uses small droplets of DEHS (di-2-ethylhexyl-sebacat) as seeding particles with an average diameter of roughly 1 µm, which are injected into the flow via jets located within the settling chamber of the wind tunnel to ensure homogenous seeding in the test section. The flow around the model is illuminated at the measurement plane using a double-pulsed 200 mJ Nd:YAG laser with a wavelength of 532 nm. Two pulses are fired with time separations of $\Delta t = 2.8$ - $9.4\,\mu\mathrm{s}$ according to the current FoV (field-of-view) and Mach number. Two measurement planes are chosen, respectively located at the model's strake (i.e., S_1 at $x/c_{\mathrm{r,w}} = 0.83$) and its main wing (i.e., S_2 at $x/c_{\mathrm{r,w}} = 1.36$) - cf. Figs. 2 and 4, so as to capture characteristic streamwise vortex-flow systems. For some cases, a third

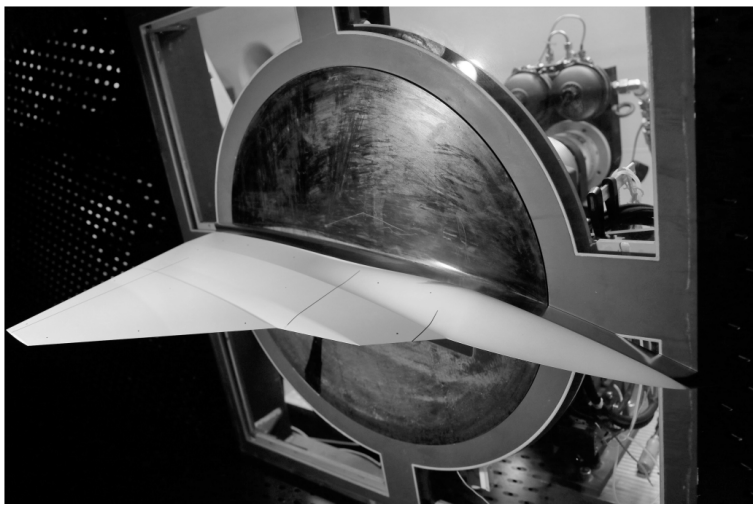

Fig. 3 Image of the DLR-F23 test model installed via its peniche in the test section of the DNW-TWG wind tunnel.

plane that follows along the strake's leading edge is also measured (see S_3 in Fig. 2), with the aim of identifying any vortex-induced crossflows. Snapshots of the flash-illuminated instantaneous flow fields are obtained via three sCMOS (scientific complementary metal-oxide-semiconductor) double-shutter cameras (PCO edge 5.5) with a resolution of 2560×2160 pixels, which are placed outside of the closed tunnel vein just behind two side-wall windows. These could be used for a stereoscopic image recording for each measurement plane S_1, S_2, and S_3. The cameras' FoVs measure $0.42\,\mathrm{m} \times 0.35\,\mathrm{m}$, $0.31\,\mathrm{m} \times 0.25\,\mathrm{m}$, and $0.40\,\mathrm{m} \times 0.23\,\mathrm{m}$ for planes S_1, S_2, and S_3, respectively. To prevent background noise in the PIV images the DLR-F23 model has been painted by a black acrylic paint.

For each test case, 1000 (double) images are recorded at a sampling frequency of $f_s = 15\,\mathrm{Hz}$, which are processed using in-house developed PIV software. For the calibration of each camera view, the PIV images are resampled in a pre-processing step, whereas distortions as well as disparities between each stereo pairing are suppressed. Then, the rectified PIV images are evaluated using a multi-grid cross-correlation algorithm with image deformation [30]. The resulting spatial resolutions in the velocity vector fields are about 4 mm for the measurement planes S_1 and S_2 and about 3 mm for S_3, whereas the velocity uncertainties are about 4 to $5\,\mathrm{m\,s^{-1}}$, 3 to $4\,\mathrm{m\,s^{-1}}$, and 5 to $10\,\mathrm{m\,s^{-1}}$ for the planes S_1, S_2, and S_3, respectively. Although the seeding particles are very small, with increasing Mach number the seeding concentration within vortex cores can decrease due to centrifugal forces acting on the droplets that in some cases can lead to missing data within the cores of strong vortices.

Fast-response, unsteady pressure-sensitive paint (uPSP) is employed to visualize the near-surface flow characteristics, providing optical measurements of unsteady pressure changes with high spatial and temporal resolution. The method is fundamentally based upon the photoluminescence of organic molecules in a polymer matrix, thus making it ideal to be applied to complex model geometries such as the DLR-F23 configuration. The paint used here was previously developed by the DLR in cooperation with the University of Hohenheim [31]. It consists of a polymer/ceramic base layer underneath an active coating. The base layer comes as a blend of a specific polymer (Duromax B-1000), ceramic particles (titanium silicon oxide TiSiO4 of 50 nm size), a dispersant, and distilled water [32], whereas its active counterpart is a mixture of toluene and PtTFPP as the luminophore [33]. This paint layers are applied *in-situ* to the model surface using a spray gun, allowing for a total paint layer thickness of only $20\,\mu\mathrm{m}$. To obtain the unsteady pressure distribution over the surface, the intensity method is used, which relies on the continuous excitation of the paint by a UV light source. A ultra-high-speed camera (Photron Mini AX 200) with a 12-bit CMOS sensor, a Canon 24 mm lens, and a band-pass filter (for wavelengths of 600 and 700 nm) is then employed to capture the light emissions. The camera is capable of recording images with a 1024 x 1024 pixels resolution, at a frame rate of 3200 Hz. Five high-power LEDs are used to illuminate the wing model, which are designed to emit light with a central wavelength of 490 nm. Each of these LEDs is applied a band-pass filter (385ET70) for a desired wavelength range (i.e., 350 to 420 nm). Finally, it is worth noting that the uPSP camera and light source are also located outside the tunnel vein behind the optical side-wall windows, i.e., akin to the PIV setup.

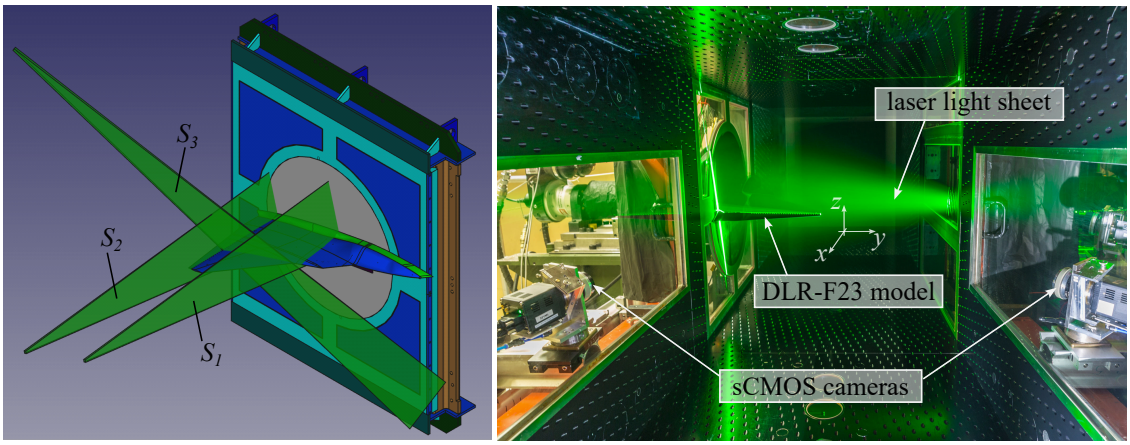

Fig. 4 Stereo-PIV setup. Images depicting the orientation of all measurement planes virtually (left) and exemplified for one test setup in the tunnel vein - see S_1 (right).

D. Experimental matrix

During the experimental campaign within the project *Diabolo*, a large test matrix is covered, comprising various flow conditions (i.e., Mach numbers and pitch angles). Seven flow speeds are considered, corresponding to Mach numbers from Ma = 0.55 to 1.15, thereby encompassing various sub- and transonic regimes. For each Mach-number case, the model is set at several incidences, with pitch angles ranging from $\alpha = 9°$ to 24° by increments of 3°. Notably, this range of incidences varies depending on the Mach number tested; In particular, for high-Mach-number flows (beyond Ma $\geq$ 1.0), the model is limited to relatively lower angles of attack due to the increased blockage and structural loads. The variation in the model's pitch angle is achieved using a hydraulically driven, high-precision actuator, placed outside the test section where the DLR-F23 configuration is mounted.

IV. Results and Discussion

In this section, the experimental results characterizing the DLR-F23 wing's vortex-flow phenomena are discussed and analyzed, their sensitivity towards the flow regime and incidence being particularly looked upon.

A. Vortex-flow phenomena on a triple-delta wing

First, the flow field occurring on and around the DLR-F23 model is characterized for a (moderate) subsonic flow (i.e., Ma = 0.65) when set at a pitch angle of 18°, thereby exploring the vortex systems before they may be significantly affected by transonic effects (e.g., compressibility). Figure 5 combines PIV and uPSP results at this particular flow condition, depicting non-dimensional axial vorticity contours ($\omega_x l_\mu / U_\infty$) and reversed flow features ($u/U_\infty < 0$) in the two measurement planes perpendicular to the inflow, with time-averaged pressure distributions (here $C_{\text{p,rms}}$ and $C_{\text{p,mean}}$) projected on the wing's surface. Under these subsonic conditions, three vortical systems are seen to develop over the wing, namely an inboard (IBV), midboard (MBV), and outboard (OBV) vortex which respectively originate from the wing's forebody, strake, and main wing. These observations are in good agreement with those from prior works; For instance, vortices developing over the strake and main wing of a triple-delta-wing configuration, respectively labeled IBV and MBV, are also reported for subsonic inflow speeds [11, 12]. Notably, however, these vortices related to the strake and main wing rather correspond to the here observed MBV and OBV. This is likely due to the present inboard vortex, IBV, either being referred to as forebody vortex instead or being not developed in the literature flow conditions. The latter may be due to the comparatively lower subsonic inflow speeds (e.g., Ma $\leq$ 0.2), for which this inboard vortex system may not have emerged, at least significantly. Aside from this, it can be seen how the present MBV and OBV change in size, vortex-core location, and vorticity magnitude when traveling further downstream (i.e., from the kink to the trailing-edge, or from PIV planes S_1 to S_2). Downstream over the main wing, the vortices appear to be broken down due to their relatively weaker, yet larger area. Besides, the IBV seems to have disappeared and/or merged with the MBV. In addition, some secondary, counter-rotating vortices are seen to develop near the leading edges of the strake and main wing, which both form underneath the larger MBV and OBV, respectively. Finally, one may also notice a region of

reversed flow, which develops in the OBV's core and indicates its broken-down state.

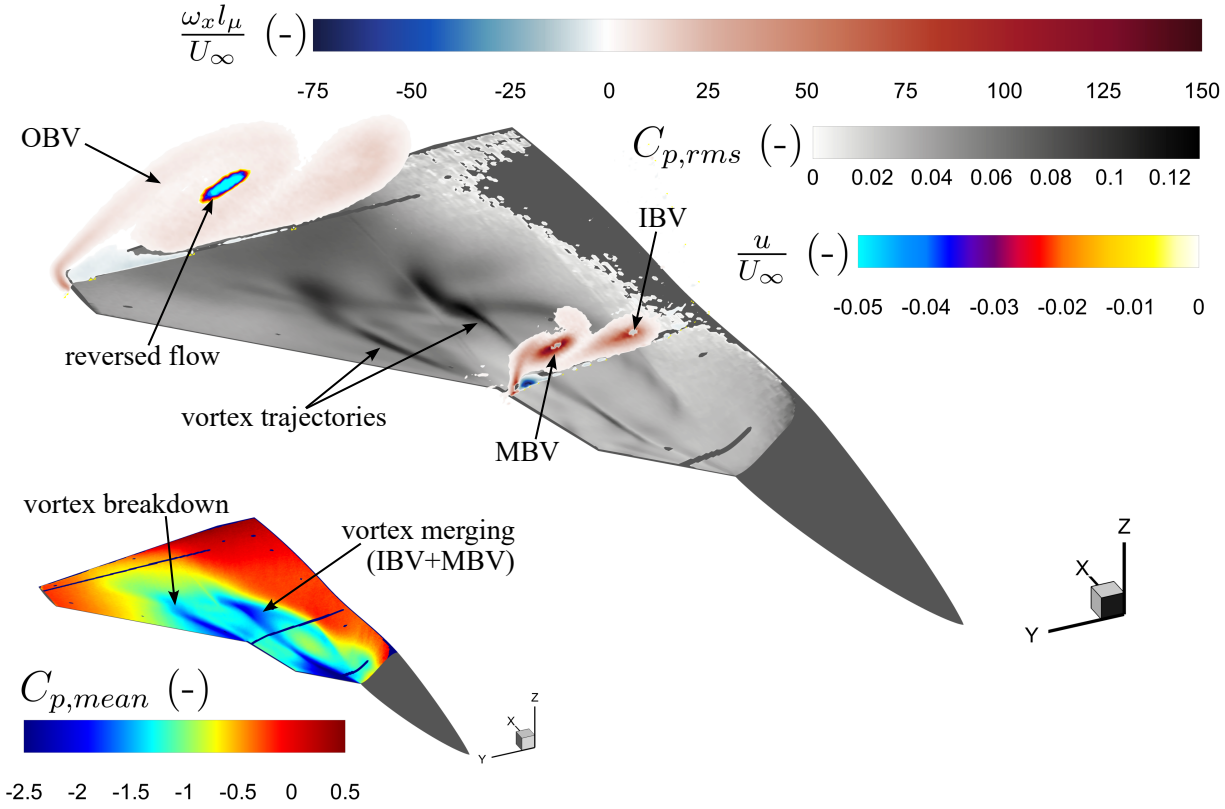

Fig. 5 Isometric view of the DLR-F23 configuration at a pitch angle α = 18° and under high-subsonic flow conditions (i.e., Ma = 0.65), depicting non-dimensional axial vorticity and reversed-flow velocities at two PIV planes as well as root-mean-square (rms) and mean pressure coefficients over the wing's surface.

When now complementing the near-wall pressure fluctuations obtained from the uPSP measurements, the cores of all three vortex systems (where the $C_{\text{p,mean}}$ values are lowest) can be tracked over the wing surface; In fact, this indicates how the IBV is drawn into the MBV, ultimately merging into one vortex. At the same time, the OBV is seen to develop at the kink between the strake's and the main wing's leading edge. The vortices' breakdown seems to occur at the location, where the high pressure fluctuation subside. At first glance, it is worth noting that the vortex core locations seem to match well between the PIV and uPSP results, as revealed by the IBV's and MBV's trajectories on the surface running through the center of the vorticity fields in the PIV plane.

After characterizing the vortical flow structures developing at subsonic conditions, Fig. 6 depicts the PIV and uPSP results under a fully transonic flow (i.e., Ma = 0.85) when set at incidence of 21°, showing non-dimensional axial vorticity contours and reversed flow features in the two measurement planes perpendicular to the inflow, again with time-averaged pressure distributions projected on the wing's surface. Please note that, for this particular case, the third PIV measurement plane (S_3) is also captured, which here depicts the normalized crossflow component (i.e., v/U_∞). Compared with its subsonic (Ma = 0.65) counterpart, the transonic case exhibits weaker vortex systems, as shown by their lower values in non-dimensional axial vorticity. In contrast, however, the reversed flows developing in the vortex cores become more pronounced, whilst also occurring in both up- and downstream planes, as for example seen for the IBV's core at the kink. Notably, a similar reversed flow may also be present in the MBV's core, which however is not resolved owing to the possible lack of tracer particles in the vortex cores with increasing flow speed (cf. III). In terms of the vortices' development, it can be seen that their structures are here even further broken down near the wing's trailing edge, with only the outer vortex bounds being visible. This is likely due to the influence of transonic effects, e.g.

the emergence of normal shocks, that would induce shock-vortex interactions. Indeed, as can be seen from the uPSP results, shock fronts develop near the kink between the LEVCON and the strake, as well as another downstream where the high surface pressure fluctuations of the vortex cores abruptly subside. The latter shock can be seen in the third (non-perpendicular) PIV plane, which plots the crossflow component; Here, a subtle "cut" in the region of increased v-velocity can be observed. Notably, it appears that, under these transonic conditions, the vortices do not merge any longer, but rather directly break down, whether this is related to their detachment or the influence by the shock fronts.

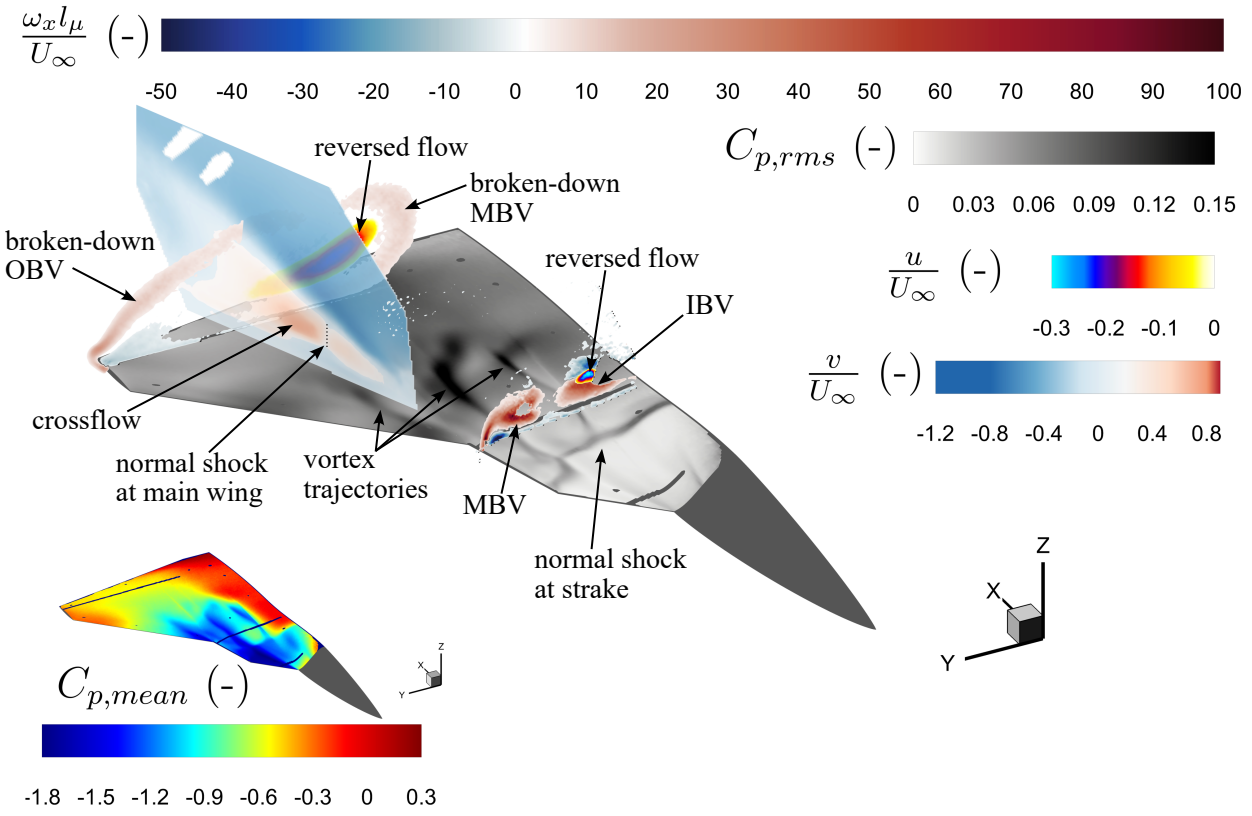

Fig. 6 Isometric view of the DLR-F23 configuration at a pitch angle $\alpha = 21°$ and under transonic flow conditions (i.e., Ma = 0.85), depicting non-dimensional axial vorticity and reversed-flow velocities at two PIV planes as well as root-mean-square (rms) and mean pressure coefficients over the wing's surface.

Next, Fig. 7 depicts the PIV and uPSP results under a high-transonic, or low-supersonic, flow (i.e., Ma = 1.15) when set at an incidence of 12°, showing non-dimensional axial vorticity contours in the two measurement planes perpendicular to the inflow, with the time-averaged pressure distributions projected on the wing's surface. At this stage, the reader is to note two aspects; first, at this higher flow speed, no reversed axial flows occur, according to which they are not plotted. Second, the pitch angle is purposely chosen to be lower (i.e., $\alpha = 12°$) compared to the previous cases, owing to the higher aerodynamic loads acting upon the wing model. Overall, it can be seen how the flow field is noticeably affected and driven by compressible effects, such as more pronounced shocks. The most striking observation is that the OBV is considerably impacted at these conditions; Here, the OBV seems to be suppressed due to the presence of a shock front that runs almost parallel to the inflow (here denoted as crossflow shock). Due to this shock behavior, the outer part of the main wing exhibits low mean pressures and the flow wrapping around its tip remain rather close to the wing surface. Contrasting the OBV, the IBV and MBV both still emerge, even though their size appears to be smaller. In terms of their vortex trajectories, they travel fairly straight in the streamwise direction, which is believed to stem from the high axial velocities compared to any lateral ones associated with the model's inboard geometry or its three-dimensional tip effects.

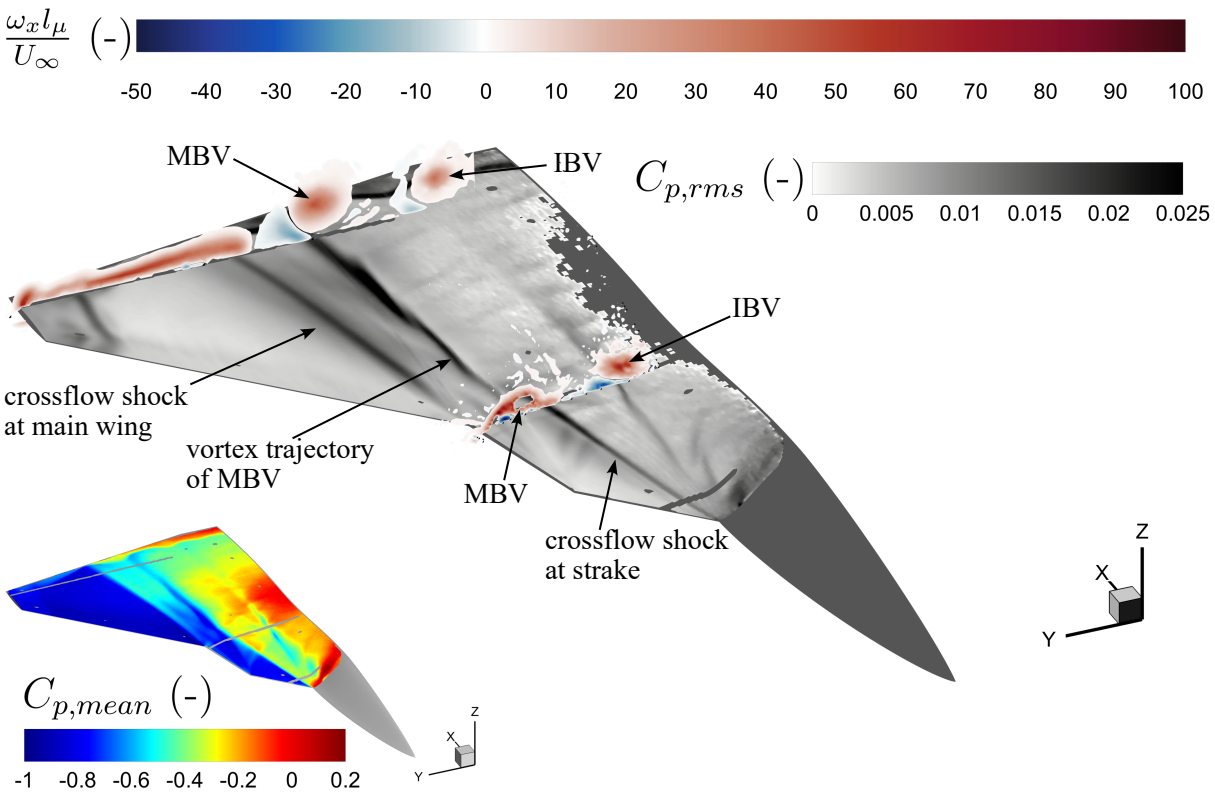

Fig. 7 Isometric view of the DLR-F23 configuration at a pitch angle α = 12° and under high-transonic flow conditions (i.e., Ma = 1.15), depicting non-dimensional axial vorticity and reversed-flow velocities at two PIV planes as well as root-mean-square (rms) and mean pressure coefficients over the wing's surface.

B. Sensitivity towards the flow regime and incidence

Upon the above observations, it is shown how susceptible these complex vortical-flow phenomena are to the flight conditions, such as the Mach number and pitch angle. To further investigate the vortices' dependency on both the flow regime and incidence, Fig. 8 depicts two-dimensional views onto the PIV planes for two selected series: for all Mach numbers tested at a fixed pitch angle (α = 12°) and across all incidences for one transonic flow regime (Ma = 0.85). Once again, the figure plots the non-dimensional axial vorticity contours alongside the regions of reversed flow, which is now complemented with markers indicating the vortices' core location derived from the flow streamlines. Please note that square and diamond markers respectively represent the vortices' core projections on the upstream (S_1) and downstream (S_2) planes. Overall, it can be seen how the vortices develop from the upstream plane (at the kink) towards the plane near the trailing-edge (over the main wing); Both the IBV and MBV move further outboard, following the DLR-F23 geometry, whilst also increasing (resp. decreasing) in terms of area (resp. vorticity magnitude). When looking at the variation in Mach number, one can observe how all three vortices shift with increasing flow speed; In particular, the OBV travels inboard, widening and eventually interacting with the MBV at Ma = 0.95, before being strongly affected by the developing crossflow shocks (at Ma > 1.0). At these higher Mach numbers, even though the OBV appears to be broken down and suppressed by the presence of the shocks, the flow streamlines revealed a vortex core that forms above the crossflow shock line. At this stage, it is also worth noting that the OBV appears to already break down at subsonic flow conditions, as revealed by the reversed-flow region in its core. Notably, such onset of axial flow deceleration (particularly flow reversal) in the vortex core is a known indicator of vortex breakdown.

Next, focusing on the vortices' behavior subject to the aircraft pitch angle, one can notice somewhat similar trends - e.g., the vortices here shift with increasing pitch angle. More importantly however, they expand away from the model

surface, significantly widening and thus interacting with one another, such that they break down (e.g., for the OBV) and/or merge (i.e., IBV, MBV, and eventually OBV) over the main wing. For instance, the vortices seem to blur together as early as $\alpha \geq$ 15-18°, with the OBV being broken down across all incidences considered. Interestingly, it is worth noting how the MBV exhibits a rather sudden breakdown behavior, characterized by a large region of strong flow reversal (see $\alpha \geq 21°$). Such an abrupt bursting appears to resemble the bubble-type vortex breakdown, according to which vortices developing from slender leading-edge geometries (i.e., $\varphi > 65°$) at high pitch angles experience a sudden stagnation of axial flow and possible flow reversal, in form of a quasi-axisymmetric bubble. Even though the sudden vortex breakdown onset is difficult to verify due to the present angular increments of 3°, the results tentatively echo the bubble-type characteristic frequently referred to in the literature [19, 20]. Finally, the IBV also exhibits rather sudden flow reversal, which occurs already upstream at the kink for high pitch angles.

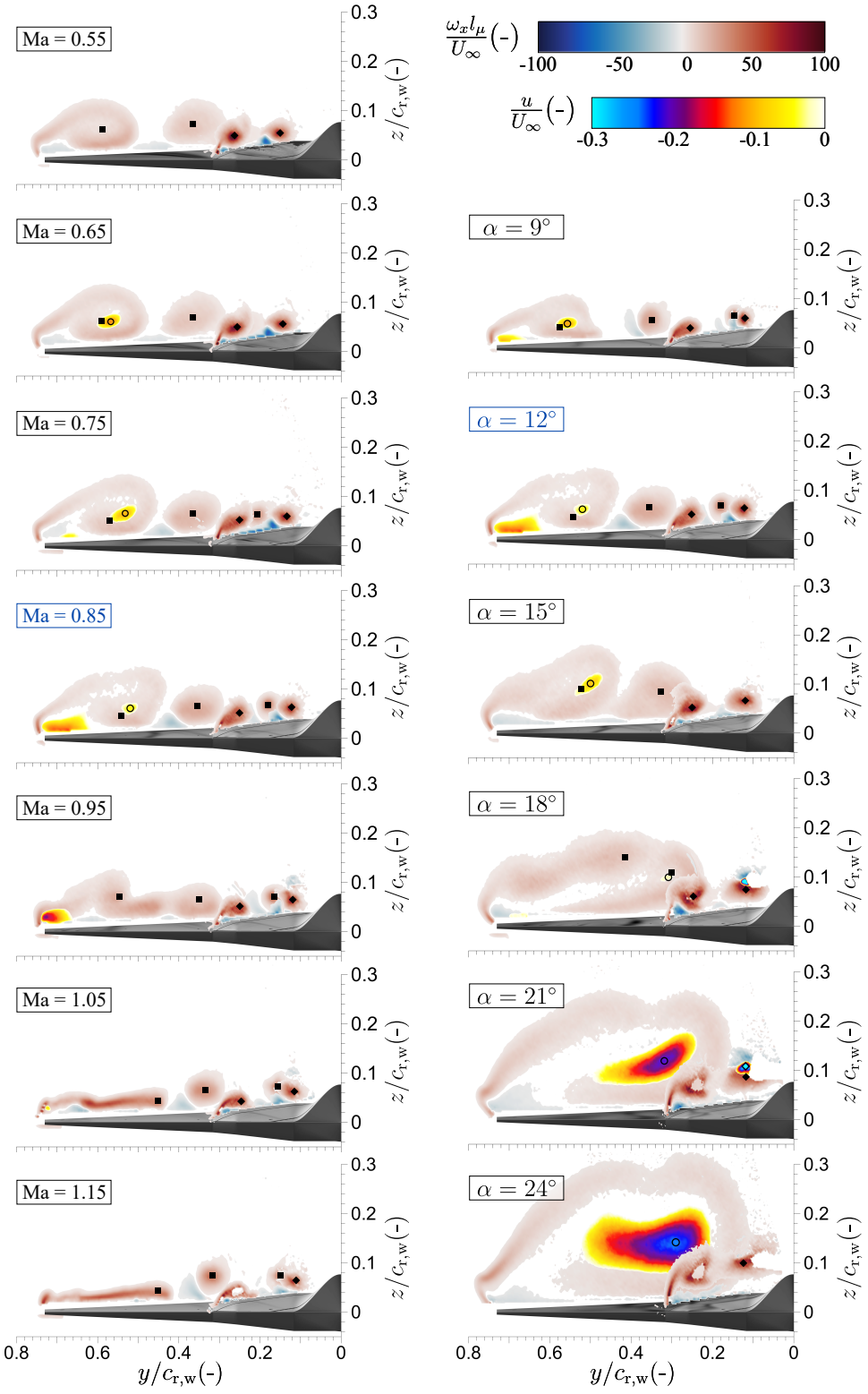

Fig. 8 Planar (2D) views of both PIV planes (S_1 and S_2) when looking downstream onto the DLR-F23 configuration, depicting non-dimensional axial vorticity and reversed-flow velocities - this being either shown for all Mach numbers (Ma = 0.55 to 1.15) at a pitch angle $\alpha = 12°$ on the left, or for all incidences ($\alpha = 9°$ to $24°$) under a fixed transonic flow speed (Ma = 0.85) on the right. Filled squares and diamonds, and hollow circles respectively indicate the vortices' cores, derived from the flow streaklines and most pronounced reversed flow.

Upon all above, the vortex dynamics driven by the flow conditions indicate rather varying vortex-core trajectories, which is looked upon in more detail in Fig. 9. The figure plots the vortices' trajectories for two selected cases in terms of Mach number and incidence, which is obtained by tracing the minimum mean pressure coefficients from the uPSP results. In addition, the vortex core locations derived from the PIV planes are projected onto the wing surface.

Fig. 9(a) depicts the trajectories of all three primary vortex systems (i.e., IBV, MBV, and OBV) across all Mach regimes at a common pitch angle of $\alpha = 12°$. As can be seen, all vortices slightly shift further inboard as the flow speed increases. This may likely contribute to earlier or delayed vortex merging, that is observed previously for the IBV and MBV. Aside from that, the MBV seems to follow more closely the LEVCON, as the Mach number increases. This may stem from the increased axial flow velocities, which leads to the shear layer just rolling up into the MBV once the kink from LEVCON to strake occurs. Regarding the vortex core projections, the PIV and uPSP show an overall fair alignment, whilst - more importantly - capturing the qualitative trend of the vortices' shift with an increasing inflow speed. What concerns the downstream PIV plane, the results are less definitive owing to the difficulty of identifying the vortices' trajectories from the surface pressures beyond their breakdown and/or merging onsets. At this stage, it is worth noting that the core locations derived from the streamlines and reversed-flow regions differ more or less significantly, both in terms of their spanwise location (what is plotted here) as well as their vertical position (cf. Fig. 8).

Next, when looking at a transonic flow case (Ma = 0.85) across all incidences in Fig. 9(b), it is most striking how the IBV and MBV develop; As can be seen, they begin to merge once the wing is pitched to an angle of attack of approximately 18°. At smaller incidences, both vortices travel downstream, before they are broken down due to the interaction with a near-trailing-edge shock front. In contrast, when pitched to higher angles, the vortices are affected by a shock front developing further upstream as well as the earlier flow detachment associated with these high angles, all resulting in the IBV and MBV breaking down before they could merge. Notably, it was also found that this critical incidence, at which the vortex merging first occurs, changes with the flow regimes; For instance, at lower Mach numbers (Ma = 0.65 and 0.75), the IBV and MBV start to merge when the model is set at $\alpha = 15°$. For the sake of conciseness, however, these other vortex trajectories are not plotted here. In terms of the vortex core projections from the PIV planes, similar trends can be observed, with their agreement being more or less promising from a qualitative or quantitative perspective, respectively.

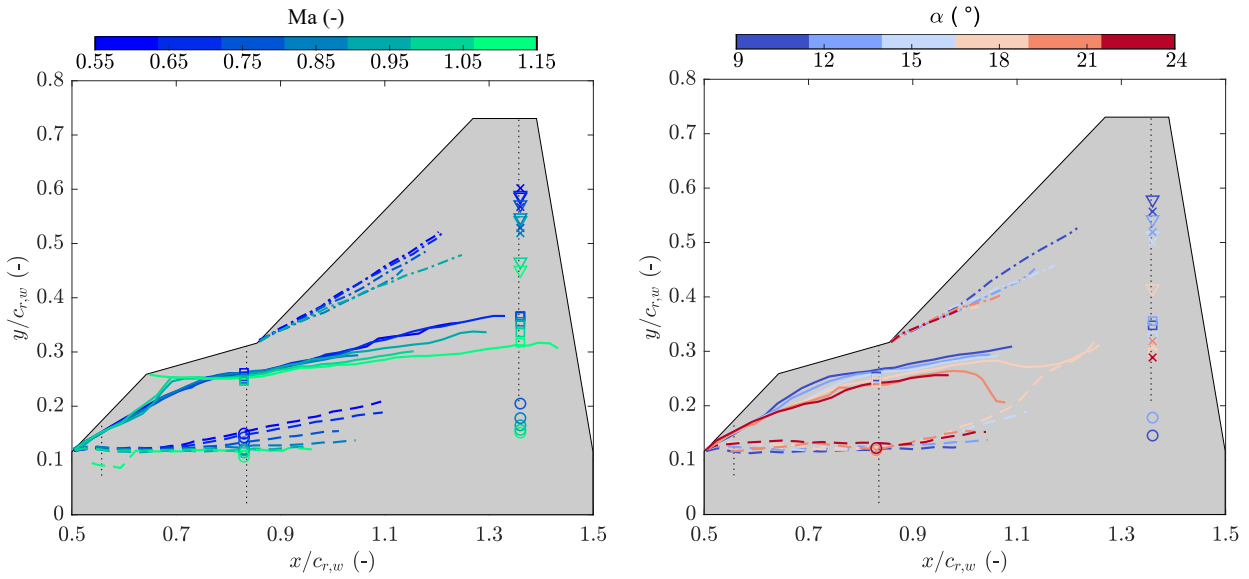

(a) Dependency on the Mach number, Ma

(b) Dependency on the angle of attack, α

Fig. 9 Dependency of the vortex trajectories with respect to the Mach number (left) and pitch angle (right). Vortex cores are projected based upon flow streaklines from the PIV results, indicated via markers for the IBV (○), MBV (□), and OBV (▽). In some cases, vortex cores are also projected using the most pronounced flow reversal (via ×).

V. Conclusions and Perspectives

The present work explored the flow field characteristics, and more specifically the vortex-flow phenomena of a generic triple-delta wing configuration, namely the DLR-F23 aircraft, in the Transonic Wind Tunnel in Göttingen. The flow structures are visualized using a combination of stereo particle-image velocimetry and fast-response, unsteady pressure-sensitive paint. To cover a large experimental matrix, a wide range of flow conditions is explored, including various flow regimes (from Ma = 0.55 to 1.15) and angles of attack (from α = 9 to 24°). Results revealed that the flow field over the DLR-F23 configuration is primarily characterized by three dominant vortex systems, namely the inboard, midboard, and outboard vortex, their trajectories and characteristics being heavily dependent on the flow regime (whether low-, medium-, or high-transonic) and/or the incidence. Aside from that, once the flow regime becomes sufficiently transonic, compressibility effects are seen to play major role in the development, merging, and breaking down of those vortical systems. Interestingly, these compressibility effects (e.g., shock fronts) develop in several regions, such as near the LEVCON/strake, further downstream near the trailing edge, and even as a crossflow shock almost parallel to the inflow. According to their complexity and variability depending on the flow conditions, further explorations of these vortex-flow phenomena in transonic regimes is highly sought after. In particular, this set of experimental data may be further used to validate numerical computations, thereby paving the way to more detailed and extensive analysis of the flow field characteristics and vortex structures. Ultimately, this would all lead to developing more efficient and high performant triple-delta-wing aircraft configurations that could operate robustly in a wide range of flight conditions (i.e., Mach numbers, pitch angles).

Acknowledgments

The authors would like to express their gratitude to all colleagues of the Institute of Aeroelasticity and Institute of Aerodynamics and Flow Technology at the DLR for their contributions in the experimental setup and data acquisition during the *Diabolo* wind tunnel test campaign, as well as their efforts towards the data curation and pre-processing. The authors would also like to thank the team of the Transonic Wind Tunnel Göttingen for their support during the experimental tests.

References

[1] Hoeijmakers, H. W. M., Vaatstra, W., and Verhaagen, N. G., "Vortex flow over delta and double-delta wings," *Journal of Aircraft*, Vol. 20, No. 9, 1983, pp. 825–832. https://doi.org/10.2514/3.44949, URL https://arc.aiaa.org/doi/10.2514/3.44949.

[2] Ekaterinaris, J., and Schiff, L., "Vortical flows over delta wings and numerical prediction of vortex breakdown," *28th Aerospace Sciences Meeting*, American Institute of Aeronautics and Astronautics, Reno,NV,U.S.A., 1990. https://doi.org/10.2514/6.1990-102, URL https://arc.aiaa.org/doi/10.2514/6.1990-102.

[3] Gursul, I., "Recent developments in delta wing aerodynamics," *The Aeronautical Journal*, Vol. 108, No. 1087, 2004, pp. 437–452. https://doi.org/10.1017/S0001924000000269, URL https://www.cambridge.org/core/product/identifier/S0001924000000269/type/journal_article.

[4] Gursul, I., Gordnier, R., and Visbal, M., "Unsteady aerodynamics of nonslender delta wings," *Progress in Aerospace Sciences*, Vol. 41, No. 7, 2005, pp. 515–557. https://doi.org/10.1016/j.paerosci.2005.09.002, URL https://linkinghub.elsevier.com/retrieve/pii/S037604210500103X.

[5] Furman, A., and Breitsamter, C., "Turbulent and unsteady flow characteristics of delta wing vortex systems," *Aerospace Science and Technology*, Vol. 24, No. 1, 2013, pp. 32–44. https://doi.org/10.1016/j.ast.2012.08.007, URL https://linkinghub.elsevier.com/retrieve/pii/S1270963812001290.

[6] Hövelmann, A., Grawunder, M., Buzica, A., and Breitsamter, C., "AVT-183 diamond wing flow field characteristics Part 2: Experimental analysis of leading-edge vortex formation and progression," *Aerospace Science and Technology*, Vol. 57, 2016, pp. 31–42. https://doi.org/10.1016/j.ast.2015.12.023, URL https://linkinghub.elsevier.com/retrieve/pii/S1270963815300250.

[7] Wiggen, S., Mai, H., Nuhn, J., Büte, T., Klein, C., Henne, U., Sachs, W., Konrath, R., and Wrede, B., "Motion-Induced Unsteady Aerodynamic Loads with Development of Vortical Flow," *Journal of Aircraft*, Vol. 55, No. 1, 2018, pp. 173–183. https://doi.org/10.2514/1.C034308, URL https://arc.aiaa.org/doi/10.2514/1.C034308.

[8] Hitzel, S., "Sub- and Transonic Vortex Breakdown Flight Condition Simulations of the F-16XL Aircraft," *Journal of Aircraft*, Vol. 54, No. 2, 2017, pp. 428–443. https://doi.org/10.2514/1.C033246, URL https://arc.aiaa.org/doi/10.2514/1.C033246.

[9] Hitzel, S., "High-Angle-of-Attack F-16XL Flight Simulations at Sub- and Transonic Speeds," *Journal of Aircraft*, Vol. 54, No. 6, 2017, pp. 2014–2026. https://doi.org/10.2514/1.C034025, URL https://arc.aiaa.org/doi/10.2514/1.C034025.

[10] Pfnür, S., Hövelmann, A., Sedlacek, D., and Breitsamter, C., "Vortex Flow Interaction Phenomena on Multi Swept Delta Wings at Subsonic Speeds," Technical Report, 2019.

[11] Pfnür, S., and Breitsamter, C., "Stereo-PIV Measurements of Vortex-Interaction Effects on Generic Delta Wing Planforms," *13th International Symposium on Particle Image Velocimetry*, Munich, Germany, 2019, p. 10.

[12] Sedlacek, D., Biechele, S., and Breitsamter, C., "Numerical investigations of vortex formation on a generic multiple-swept-wing configuration," *CEAS Aeronautical Journal*, Vol. 13, No. 1, 2022, pp. 295–310. https://doi.org/10.1007/s13272-021-00566-y, URL https://link.springer.com/10.1007/s13272-021-00566-y.

[13] Ghoreyshi, M., Fagley, C., and Seidel, J., "Vortex Interaction Characteristics of Multiswept Wings at Subsonic Speeds," *AIAA Journal*, Vol. 61, No. 7, 2023, pp. 2932–2947. https://doi.org/10.2514/1.J062605, URL https://arc.aiaa.org/doi/10.2514/1.J062605.

[14] Ghoreyshi, M., Fagley, C., and Seidel, J., "Aerodynamic flow field analysis of vortex interactions on multi-swept wing configurations," *Aerospace Science and Technology*, Vol. 150, 2024, p. 109215.

[15] Stegmüller, J., Molz, A., García-Guillén, P., and Breitsamter, C., "Flow field analysis of a high agility type aircraft aeroelastic wind tunnel model," *Aerospace Science and Technology*, Vol. 162, 2025, p. 110177.

[16] Delery, J. M., "Aspects of vortex breakdown," *Progress in Aerospace Sciences*, Vol. 30, No. 1, 1994, pp. 1–59. https://doi.org/10.1016/0376-0421(94)90002-7, URL https://linkinghub.elsevier.com/retrieve/pii/0376042194900027.

[17] Breitsamter, C., "Unsteady flow phenomena associated with leading-edge vortices," *Progress in Aerospace Sciences*, Vol. 44, No. 1, 2008, pp. 48–65. https://doi.org/https://doi.org/10.1016/j.paerosci.2007.10.002, URL https://www.sciencedirect.com/science/article/pii/S0376042107000796.

[18] Hirschel, E. H., Rizzi, A., Breitsamter, C., and Staudacher, W., *Separated and Vortical Flow in Aircraft Wing Aerodynamics: Basic Principles and Unit Problems*, Springer Nature, 2020.

[19] Lambourne, N., and Bryer, D., "The bursting of leading-edge vortices-some observations and discussion of the phenomenon," 1961.

[20] Visbal, M. R., "Onset of vortex breakdown above a pitching delta wing," *AIAA Journal*, Vol. 32, No. 8, 1994, pp. 1568–1575. https://doi.org/10.2514/3.12145, URL https://arc.aiaa.org/doi/10.2514/3.12145.

[21] Di Fabbio, T., Tangermann, E., and Klein, M., "Investigation of transonic aerodynamics on a triple-delta wing in side slip conditions," *CEAS Aeronautical Journal*, Vol. 13, No. 2, 2022, pp. 453–470. https://doi.org/10.1007/s13272-022-00571-9, URL https://link.springer.com/10.1007/s13272-022-00571-9.

[22] Di Fabbio, T., Tangermann, E., and Klein, M., "Investigation of Reynolds stresses prior to vortex breakdown on a triple-delta wing at transonic condition," *12th International Symposium on Turbulence and Shear Flow Phenomena*, Osaka, Japan, 2022, p. 6.

[23] Werner, M., Rein, M., Richter, K., and Weiss, S., "Experimental and numerical analysis of the aerodynamics and vortex interactions on multi-swept delta wings," *CEAS Aeronautical Journal*, Vol. 14, No. 4, 2023, pp. 927–938. https://doi.org/10.1007/s13272-023-00678-7, URL https://link.springer.com/10.1007/s13272-023-00678-7.

[24] Jeans, T. L., McDaniel, D. R., Cummings, R. M., and Mason, W. H., "Aerodynamic Analysis of a Generic Fighter Using Delayed Detached-Eddy Simulation," *Journal of Aircraft*, Vol. 46, No. 4, 2009, pp. 1326–1339. https://doi.org/10.2514/1.40955, URL https://arc.aiaa.org/doi/10.2514/1.40955.

[25] Rajkumar, K., Fabbio, T. D., Tangermann, E., and Klein, M., "Physical aspects of vortex-shock dynamics in delta wing configurations," *Physics of Fluids*, Vol. 36, No. 6, 2024, p. 066112. https://doi.org/10.1063/5.0213122, URL https://doi.org/10.1063/5.0213122.

[26] Di Fabbio, T., Rajkumar, K., Tangermann, E., and Klein, M., "Towards the understanding of vortex breakdown for improved RANS turbulence modeling," *Aerospace Science and Technology*, Vol. 146, 2024, p. 108973.

[27] Werner, M., Schütte, A., and Weiss, S., "Turbulence Model Effects on Vortex Interaction Prediction on a Multiswept Delta Wing," *Journal of Aircraft*, Vol. 61, No. 1, 2024, pp. 211–221.

[28] Zastrow, J., Oberdieck, F., Henne, U., and Klein, C., "Numerical and Experimental Investigations on the DLR-F23 Combat Aircraft Wind Tunnel Model," *33rd Congress of the International Council of the Aeronautical Sciences*, International Council of the Aeronautical Sciences (ICAS), Stockholm, Sweden, 2022, p. 20.

[29] Hartl, P., Ritschel, M., Braune, M., and Mai, H., "Experimental investigation of the DLR-F23 configuration at transonic speeds using fast-response pressure-sensitive paint," *34th Congress of the International Council of the Aeronautical Sciences*, International Council of the Aeronautical Sciences (ICAS), Florence, Italy, 2024, p. 21.

[30] Raffel, M., Willert, C., Scarano, F., Kähler, C. J., Wereley, S. T., and Kompenhans, J., *Particle Image Velocimetry - A Practical Guide (3rd Edition)*, Vol. 1, Springer Verlag, 2018. URL https://elib.dlr.de/119724/.

[31] Gregory, J., Sakaue, H., and Sullivan, J., "Unsteady pressure measurements in turbomachinery using porous pressure sensitive paint," *40th AIAA Aerospace Sciences Meeting & Exhibit*, American Institute of Aeronautics and Astronautics, Reno,NV,U.S.A., 2002. https://doi.org/10.2514/6.2002-84, URL https://arc.aiaa.org/doi/10.2514/6.2002-84.

[32] Gößling, J., Ahlefeldt, T., and Hilfer, M., "Experimental validation of unsteady pressure-sensitive paint for acoustic applications," *Experimental Thermal and Fluid Science*, Vol. 112, 2020, p. 109915. https://doi.org/10.1016/j.expthermflusci.2019.109915, URL https://linkinghub.elsevier.com/retrieve/pii/S0894177718320089.

[33] Puklin, E., Carlson, B., Gouin, S., Costin, C., Green, E., Ponomarev, S., Tanji, H., and Gouterman, M., "Ideality of pressure-sensitive paint. I. Platinum tetra(pentafluorophenyl)porphine in fluoroacrylic polymer," *Journal of Applied Polymer Science*, Vol. 77, No. 13, 2000, pp. 2795–2804. https://doi.org/10.1002/1097-4628(20000923)77:13<2795::AID-APP1>3.0.CO;2-K, URL https://onlinelibrary.wiley.com/doi/10.1002/1097-4628(20000923)77:13<2795::AID-APP1>3.0.CO;2-K.